FOCUS ISSUE OF SELECTED PRESENTATIONS FROM IMLB 2014

In Operando Small-Angle Neutron Scattering (SANS) on Li-Ion Batteries

Stefan Seidlmayer,[a,z] Johannes Hattendorff,[b] Irmgard Buchberger,[b] Lukas Karge,[a] Hubert A. Gasteiger,[b,*] and Ralph Gilles[a]

[a]*Heinz Maier-Leibnitz Zentrum (MLZ), Technische Universität München, 85747 Garching, Germany*
[b]*Chair of Technical Electrochemistry, Technische Universität München, 85748 Garching, Germany*

Small-angle neutron scattering is a tool providing information on nanostructures of objects in the order of 1-300 nm. In this experiment a pouch bag lithium ion battery cell was investigated with SANS ex situ, in situ and in operando during charging and discharging. $LiNi_{0.33}Mn_{0.33}Co_{0.33}O_2$ was used as cathode and graphite as anode material. The small-angle neutron scattering measurements were performed on the SANS-1 instrument at the FRM II neutron source of the Heinz Maier-Leibnitz Zentrum (MLZ) in Garching, Germany. Ex situ measurements of components of the cell as well as static in situ and dynamic in operando SANS experiments were performed with a complete Li-ion pouch bag cell. The cell was charged and discharged twice with C/3 and small-angle neutron scattering data were collected during the measurements. The observed intensity data were then evaluated and changes of the total scattering in the measured Q-range are correlated to the lithiation processes occurring inside the cell. Thus we can show that SANS can be used as a tool to monitor kinetic processes in Li-ion batteries in operando and non-destructively.
 [DOI: 10.1149/2.0181502jes]

Manuscript submitted November 3, 2014; revised manuscript received December 15, 2014. Published January 15, 2015. This was Paper 701 presented at the Como, Italy, Meeting of the IMLB, June 10–14, 2014. *This paper is part of the Focus Issue of Selected Presentations from IMLB 2014.*

Li-ion batteries have been used widely as power sources in transportable electronic devices and new markets such as hybrid and all battery electric vehicles are developing.[1] This has also raised an enhanced interest in the development of analytical methods to study batteries during operation ("in operando"). Besides the improvement in energy and power density, researchers are trying to prolong the lifetime of lithium ion batteries. Cycle and storage life of Li-ion batteries are critical for electric vehicle or stationary power storage applications. A major degradation effect is the continuous decomposition of electrolyte - leading also to a growing solid electrolyte interface (SEI), a passivating layer on typically the anode active material (graphite), thus resulting in loss of conductivity and higher cell resistance. For the cathode phase transitions, structural disorder and metal dissolution are major aging effects. Corrosion of various materials in the battery and mechanical contact loss of active particles or current collectors are also an issue.[2–4] One major goal is to understand the general reaction mechanism of the Li-intercalation process in the anode respectively cathode materials. The fundamental understanding of battery processes is a key for improving battery performance (e.g., in terms of energy density and power density) and lifetime.

The small-angle scattering method is commonly used to gain information about the nanostructure of the investigated materials (i.e., size, volume and shape of particles). In combination with the special properties of neutrons, like the high penetration depth in materials, small-angle neutron scattering (SANS) can be used as a powerful tool for in situ investigations of Li-ion batteries. SANS can help to understand changes on the nanoscale of particles in cycled cells and during cell cycling. Our study's primary goal is to adapt, develop and extend this method to Li-ion battery systems, since up to now only a few publications exist dealing with the SANS method for batteries and battery materials in general. Sandi et al.[5] and Mamun et al.[6] have studied the pore structures of raw anode materials. While Bridges et al.[7] have gained insights into the SEI formation on hard-carbon anodes with in operando SANS experiments with lithium counter electrodes. Furthermore, Nagao et al.[8] have studied the Li-intercalation mechanism into hard carbon anode materials using ex-situ SANS in combination with other methods. Also, Wang et al. recently presented a short overview on various neutron methods for investigating batteries.[9]

In situ and in operando SANS offers the possibility to study particle related nanoscale effects within fully operational Li ion cells non-destructively, without the need to disassemble the cells into single working electrodes nor to otherwise disturb the cell assembly if a suitable geometry such as a pouch bag shape of the cell can be used. This huge advantage though is tied with the problem that the resulting neutron scattering is of course a superposition of the scattering of the various battery cell parts (anode, cathode, electrolyte, separator, etc.) with nano scaled objects. This means that the resulting scattering data of this complex system has to be carefully evaluated prior to making any conclusions.

This SANS study is focused on the investigation of Li-ion cells which were characterized non-destructively during cycling (and aging). The combination of previous ex situ and in situ measurements allows drawing conclusions despite the very complex superimposed scattering data. In this article we report on in operando SANS of home-built graphite|NMC pouch bag type cells. Three types of small-angle neutron scattering data are combined to give insight into the lithium (de-)intercalation process of a graphite electrode in a full battery. First we show ex situ measurements of single battery components and investigate the individual contributions to the SANS signal. Then we compare data of complete cells in fully charged and discharged state measured in situ over the full accessible Q-range. Finally, we demonstrate how SANS can be used to monitor cell operation in operando by comparing data from a cell measured two times with a storage period between measurement runs. This article is the first in a series and will present the measurement principle as well as the data evaluation approach of a novel SANS data analysis method. Future articles will focus on in operando kinetic studies in batteries using this method. Concerning references to color in figures in this article, the reader is referred to the online version.

Experimental

Sample cell preparation.— First, the active material powders were characterized with a particle sizer (LA950, Retsch-Horiba) to measure the particle size distribution by laser scattering.

*Electrochemical Society Fellow.
[z]E-mail: stefan.seidlmayer@frm2.tum.de

Figure 1. (color online): Assembled pouch bag cell for in situ SANS. The circle shows the neutron beam size and position on the cell.

For the cathode, an NMP-based (N-methyl-2-pyrrolidone) slurry was prepared with commercially available NMC, $LiNi_{0.33}Mn_{0.33}Co_{0.33}O_2$ cathode material, PVDF-binder (Polyvinylidene fluoride, Kynar) and carbon black (C65, Timcal) as a conductive additive with solid weight fractions of 96:2:2, respectively. This slurry was coated with a doctor blade on a thin Al-foil (18 μm). The anode slurry consisted of standard artificial graphite (SGL Carbon GmbH) and PVDF with solid weight fractions of 95:5, coated onto a thin Cu-current collector foil (∼12 μm). Electrodes were dried under vacuum in a Büchi-oven prior to cell assembly in an Argon filled glove box (water content <2 ppm). The cell was assembled as a pouch bag cell with single layer cathode and anode electrodes separated by two layers of Celgard C2325 separator. Before sealing the pouch cell (consisting of a multilayer of Nylon, aluminum and polypropylene), 300 μL of 1M $LiPF_6$ dissolved in EC:EMC (3:7) were added as electrolyte. Sealing pressure in the vacuum chamber sealing device was 50 mbar.

The anode was overbalanced in terms of loading per area and also geometrically (anode size 3.5 × 3.5 cm^2, areal capacity 3.07 mAh/cm^2 calculated with a specific capacity of 372 $mAh/g_{graphite}$, thickness 98 μm) vs. cathode (cathode size 3 × 3 cm^2, areal capacity 2.53 mAh/cm^2, assuming a specific capacity of 150 $mAh/g_{(NMC)}$, thickness 97 μm). From the total amount of 152 mg cathode active material in the cell, the maximum cell capacity equates to 23 mAh at a rate of 1 C for a potential window of 3 to 4.2 V. The assembled cell type is shown in Figure 1.

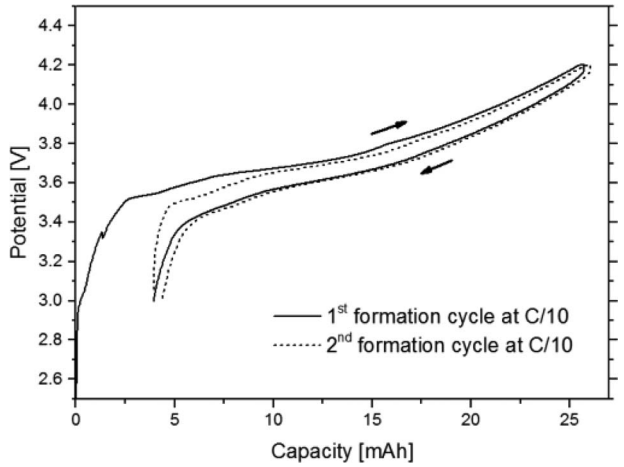

Figure 2. Two formation cycles at C/10. Charge and discharge curves shown in cyclic representation.

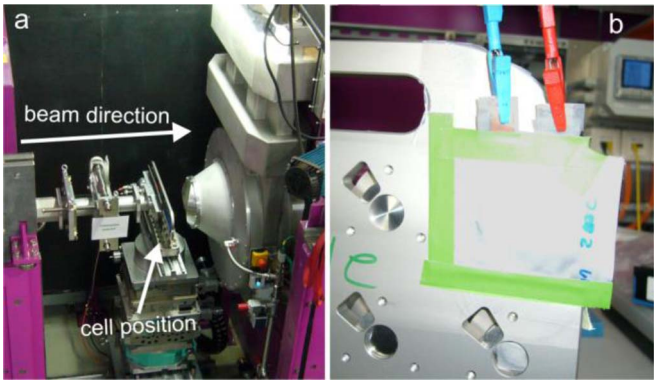

Figure 3. (color online): Mounting of the sample cell in a sample exchanger for in situ SANS measurements on the SANS-1 instrument. The image a) on the left shows the SANS-1 sample chamber. The image b) to the right shows the mounting of the pouch bag cell.

Cell formation was done by two initial charge/discharge cycles (shown in Figure 2) at a constant current (CC) rate of C/10 to 4.2 V with a constant voltage (CV) hold until the current drops to C/20, followed by a CC discharge at C/10 down to 3 V. The irreversible capacity loss in the first cycle was 3.9 mAh. Thus, the discharge capacity at C/10 reached 21.7 mAh or 142 $mAh/g_{(NMC)}$ in the second cycle, which was then set as the nominal 100% capacity in the subsequent experiments (i.e., a rate of 0.1 C corresponding to 2.17 mA). The coulombic efficiency of 98% and the rather small charge/discharge overvoltage of 40 to 50 mV at C/10 indicate overall good initial cell performance.

All experiments were carried out at room temperature. The prepared pouch bag cell was checked with impedance spectroscopy, showing a high frequency resistance of ≈1 Ω and, after formation, a Nyquist-diagram with two semi-circles results, which is typical for this type of cell chemistry after SEI formation.[10]

Small-angle neutron scattering (SANS).— The ex situ samples, the static in situ cell and the dynamically operated in operando cell were mounted at the SANS-1 instrument of the FRM II neutron source at the Heinz Maier-Leibnitz Zentrum (MLZ) in Garching[11–13] (see Figure 3).

The instrument allows the selection of a wavelength λ within the range of 4.5 Å–20 Å with a wavelength spread of $\Delta\lambda/\lambda = 10\%$ through a mechanical velocity selector. For our measurements we used a mean wavelength of 6 Å. The final aperture before the sample reduced the neutron beam to a radial diameter of 8 mm before impinging on the sample. The instrument schematics are displayed in Figure 4.

Scattered neutrons were recorded with a ^{3}He position-sensitive proportional counter detector with 128 single tubes arranged to a 1000 × 1020 mm^2 total area and 8 mm pixel resolution (128 × 128 pixel area) with a counting rate of up to ∼1 MHz. Measured intensities were corrected for sample transmission, background intensity, and detector efficiency. In SANS the intensity is recorded as a function of the scattering vector Q which describes the directional change and momentum transfer of a neutron during scattering. The absolute value of Q is given by the scattering angle 2θ (angle between the incoming and the scattered neutron beam) and the wavelength λ according to equation:

$$\boldsymbol{Q} = 4\pi \sin(\theta)/\lambda \quad [1]$$

2θ is the scattering angle, λ is the wavelength of the neutron beam. Generally, the Q-vector can also be regarded as the yardstick at which length scale the sample is looked at. In a simple consideration with a few assumptions the absolute value of the scattering vector Q can be correlated to the size d of a particle with an estimation of particle diameter of:

$$d = \frac{2\pi}{\boldsymbol{Q}} \quad [2]$$

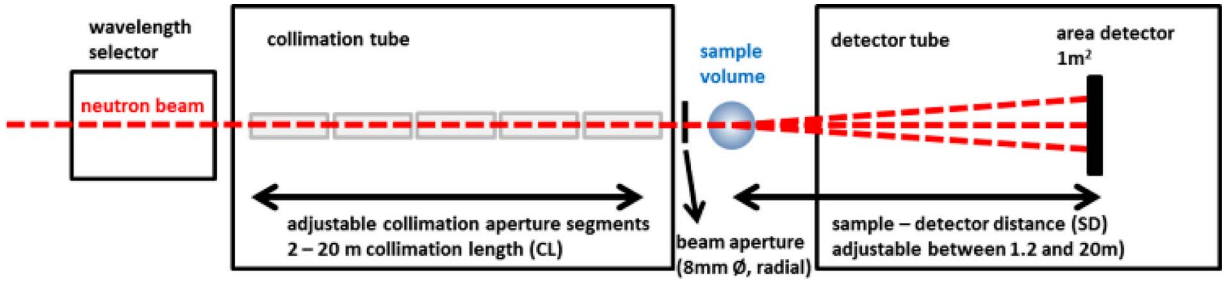

Figure 4. (color online): Schematic view of the SANS-1 instrument at the Heinz Maier-Leibnitz Zentrum (MLZ).

The scattering cross section $d\Sigma/d\Omega$, as a measure of the scattering intensity normalized by the sample volume, is then calculated according to:

$$\frac{d\Sigma}{d\Omega}(Q) = \frac{I(Q)}{I_0 t \Delta\Omega(Q) T} \quad [3]$$

I(Q) is the measured intensity within a detector pixel, $\Delta\Omega$ is the solid angle element, I_0 the intensity of the primary beam, t the sample thickness, T the sample transmission. Absolute intensities are then calculated by scaling with the incoherent scattering of a standard sample such as water with a defined thickness of 1 mm.

Three types of SANS experiments using different resolution settings were used. For the ex situ measurements of single cell components the neutron scattering data were collected and merged from setting three different resolution ranges. Similarly the static in situ measurements comparing the fully charged and discharged states were performed with the same settings. Only for the dynamic in operando measurements we restricted the resolution to the medium Q-range to increase our time resolution and focus on a certain length scale region. The following three configurations were used throughout all experiments.

I) high resolution

sample-detector distance (SDD) = 20 m
beam collimation length (CL) = 20 m
Q-range = 0.027 – 0.35 nm^{-1}

II) medium resolution

SDD = 8 m, CL = 8 m
Q-range = 0.11–0.85 nm^{-1}

III) low resolution

SDD = 1.6 m, CL = 4 m
Q-range = 0.35–4.11 nm^{-1}

For the in operando charging experiment, the SANS-1 instrument was set to the medium resolution configuration (CL = 8m, SDD = 8m and λ = 6 Å). This setting allows to access a Q-vector region in which particle scattering from 10 to 50 nm can be resolved. The wavelength of 6 Å was selected because SANS-1 has the flux maximum close to this value with a reasonable resolution, thus allowing fastest possible measurements with good statistics. Scattering data were then collected constantly during the charging in 10 min time intervals. For the charging/discharging procedures, a standard Biologic VSP-type potentiostat was connected to the cell.

After finishing the cell formation cycles, the cell was measured for one 1st cycle in operando on the SANS-1 instrument and afterwards stored under ambient conditions. The cell was also measured statically in situ in discharged and charged state before and after this cycle. After three months the cell was checked, cycled once and then measured again in the 2nd SANS cycle.

During the 1st in operando SANS measurement, the cell was charged with constant current of C/3 up to 4.2 V with a CV hold until a current cutoff of C/25. After 150 minutes under OCV conditions (open circuit voltage) the cell was discharged with a constant current of C/3 down to 3 V. After three months the cell was cycled a 2nd time at C/3 to confirm the stability prior to the repetition of the in operando SANS measurement. In the 2nd in operando SANS experiment the cell was first charged and then discharged in the same way with C/3. The SANS data were only collected during the discharge for comparison with our 1st SANS measurement. The discharge capacities of 1st and 2nd SANS cycle show aging of less than 4% over the three month storage indicating a sufficient electrochemical stability of the cell.

Results and Discussion

Scattering theory in small angle scattering.— Generally, when analyzing small-angle scattering data, the intensity or magnitude of the sample scattering is fitted with models to obtain the information about particle size, size distribution, volume fraction and shape of particles and other parameters. From the general scattering theory the scattering amplitude of a particle is given as:

$$A(Q) = \int_V \rho(r)\, e^{-iQ\cdot r}\, dr \quad [4]$$

$\rho(r)$ is the distribution function of scattering length densities and thus directly related to the chemical composition of the scattering system. The measured intensity of the scattered neutrons on the detector is then the absolute square of the amplitude normalized with the sample volume V:

$$I(Q) = \frac{A(Q)A^*(Q)}{V} \quad [5]$$

In summary, for a condensed particle scattering system consisting of homogenous isotropic scattering centers of a defined coherent scattering length density ρ dispersed in a matrix of a medium scattering length density $<\rho>$, the intensity of the scattering per volume can be generalized by the following expression according to Grillo et al. or Kostorz:[14,15]

$$I(Q) = \Phi V_p^2 \Delta\rho^2 F^2(Q) \times S(Q)$$
$$= K \Delta\rho^2 P(Q) \times S(Q) \quad [6]$$

The measured intensity is thus the product of the total neutron flux Φ, particle volume V_p, contrast factor $\Delta\rho^2$, particle form factor P(Q) and structure factor S(Q). The form factor can be regarded as the function of the shape of the scattering particles while the structure factor S(Q) describes the distribution of the particles in space and inter-particle interactions. The contrast factor $\Delta\rho^2$ is the scattering contrast resulting between the modelled particles with scattering length densities ρ and the surrounding matrix of the averaged scattering length density $<\rho>$. Particle volume is essentially constant in the course of our experiment and thus a sample and experiment specific constant K can be defined. Typically, when dealing with the scattering of a simple system the form and/or structure factor is fitted to models yielding information about the discrete particle parameters like particle shape, size, distribution etc.

From eq. 6 we can deduce that the magnitude of the scattered intensity is a function of the so called scattering length density (SLD),

Table I. Calculated scattering length densities (SLDs) for various battery materials and components using eq. 8 and the SASFit SLD-Calculator.[26]

Phase	Density in g/cm^3	SLD in 10^{10} cm^{-2}
Al	2.70	2.0785
C (Graphite)	2.27	7.5643
LiC_{12}[1]	2.31	6.9331
LiC_6[1]	2.41	6.3597
LiNMC	4.77	3.7911
$Li_{0.75}NMC$[2]	4.68	3.9291
$Li_{0.5}NMC$[2]	4.60	4.0757
Polypropylen $(CH_2)_n$ (inner hull)	0.946	−0.3379
6-Nylon ($C_6H_{11}NO$) (outer hull)	1.084	0.8025
EC, $C_3H_4O_3$	1.321	2.0227
EMC, $C_4H_8O_3$	1.01	0.8227
SEI[4]	-	1.3414
Electrolyte[3]		
EC:EMC (3:7) + 1M $LiPF_6$	1.15	1.2407

NMC = $Ni_{0.333}Mn_{0.333}Co_{0.333}O_2$, EC = Ethylcarbonate, EMC = Ethylmethylcarbonate.
[1]Calculated with crystallographic densities from neutron powder structure refinements.[27]
[2]Calculated from NMC density with molar mass adjusted to Li-content in formula.
[3]Calculated average SLD considering all components in proper mass fractions.
[4]Average SLD for the SEI components given by Bridges et al.[7]

respectively the scattering contrast $\Delta\rho$ in the form of the contrast factor $\Delta\rho^2$:

$$\Delta\rho^2 = (\overline{SLD_A} - \overline{SLD_B})^2 \quad [7]$$

In a typical SANS experiment this contrast is usually between a liquid or a matrix (SLD_A) and the particles (SLD_B) dispersed in this medium. This contrast can also be considered as the scattering from the surface of the particles, or the interface between the two systems. The SLD is a function of the atomic composition and can be calculated from the tabulated specific neutron scattering length of the corresponding nuclei and the respective atomic number density of the particle in view. For a given molecule A_iB_j the SLD hence is:[15]

$$SLD = \frac{i \times b_A \times N_A + j \times b_B \times N_A}{M\left(A_i B_j\right) \times \rho} \quad [8]$$

where b_A, b_B are the scattering length of nuclei A, B (usually tabulated in units of fermi = 10^{-13} cm), M the molar mass (g/mol) of the molecule A_iB_j, N_A the Avogadro number and ρ the mass density per volume (g/cm^{-3}).

Typical SLDs of our sample components are summarized in Table I. The scattering length density for a certain phase can be either positive or negative. Negative values mean that the scattered neutrons are phase shifted by 180°. This phase shift is visible as an additional contribution to the scattering amplitude as the contrast factor $\Delta\rho^2$ is the absolute square value (see eq. 7) of the different scattering length density values.

For a sample with complex scattering like a pouch bag cell battery, the problem arises that the obtained data are not just the scattering of a single "sample" with an effective scattering contrast factor, form and structure factor like described in eq. 6. In this case of a large macroscopic sample one has to consider that the scattering observed is a superposition of various microscopic scattering systems, but macroscopically independent scattering contributions. This can effectively be expressed as:

$$I(Q) = K\,\Sigma_i \Delta\rho_i^2 N_i P_i(Q) \times S_i(Q) \quad [9]$$

Each part i of the superposition is the description of an independent system of scattering centers which are otherwise largely separated from each other within the sample. In our case, for example the anode particles dispersed in the electrolyte are adequately distinct from the cathode particles dispersed in the electrolyte, so they can be regarded as independent scattering contributors, each of them with its own structure and form factor.

When dealing with the scattering of a complete pouch bag battery, one can still gain information from the calculated SLD and contrast factors. So let us first consider various contrast factors of the sub-scattering systems present in the pouch bag cell (see Table II). For example, it can be checked, which component i should be the major scattering contributor. We can experimentally check these values by measuring the individual components of the pouch cell under the same conditions using the same absolute intensity scaling (i.e., water). The scattering contrast factors $\Delta\rho^2$ of the respective component A vs. the electrolyte solution as component B is tabulated in Table II. Additionally, the values for LiC_6 and LiC_{12} as component A vs. LiC_{12} respectively graphite as component B are added to this list.

A typical pouch bag envelope consists of a polymer/Al metal foil composite which is normally composed of three major layers, an outer and inner polymer layer coated on both sides of a water and air tight Al-metal foil. A schematic overview of the experimental cell is shown in Figure 5.

In our case the outer pouch bag envelope (45 μm thickness each side) has roughly the same thickness as our anode and cathode active material layers, respectively. From Table II we can extrapolate that the casing will scatter only marginally (∼10%) compared to the signal we obtain from the active material layers. Also, the separator with only 2 × 25 μm thickness and a low contrast factor of only 2.49 × 10^{10} cm^{-2}

Table II. Scattering contrast factors, $\Delta\rho^2$, of combinations from cell components of interest. Idealized elemental formulas are assigned to charged, half-charged and discharge state.

component A	component B	$\Delta\rho^2 \times 10^{10}$ [cm^{-2}]	$\Delta\rho^2$ relative to largest value	difference of $\Delta\rho^2$ relative to pristine C
Anode, pristine C, discharged	Electrolyte EC:EMC(3:7) + 1M $LiPF_6$	39.99	100%	0%
Anode LiC_{12}, half-charged	Electrolyte EC:EMC(3:7) + 1M $LiPF_6$	32.40	81%	−19%
Anode LiC_6, charged	Electrolyte EC:EMC(3:7) + 1M $LiPF_6$	26.20	66%	−34%
Cathode Li_1NMC discharged	Electrolyte EC:EMC(3:7) + 1M $LiPF_6$	6.50	16%	0%
Cathode $Li_{0.75}NMC$ half-charged	Electrolyte EC:EMC(3:7) + 1M $LiPF_6$	7.23	18%	+11%
Cathode $Li_{0.5}NMC$, charged	Electrolyte EC:EMC(3:7) + 1M $LiPF_6$	8.04	20%	+24%
Polypropylene $(CH_2)_n$ = inner envelope and separator	Electrolyte EC:EMC(3:7) + 1M $LiPF_6$	2.49	6%	-
6-Nylon ($C_6H_{11}NO$) = outer envelope	Air (N_4O = 80% N, 20% O)	0.64	2%	-
SEI [Li, Li_2O, LiF, Li_2CO_3, $(CH_2OCO_2Li)_2$][1]	Electrolyte EC:EMC(3:7) + 1M $LiPF_6$	0.010	0%	-
LiC_{12}	Graphite	0.40	<1%	-
LiC_6	LiC_{12}	0.33	<1%	-

[1]calculated from average SLD for SEI components given by Bridges et al.[7]

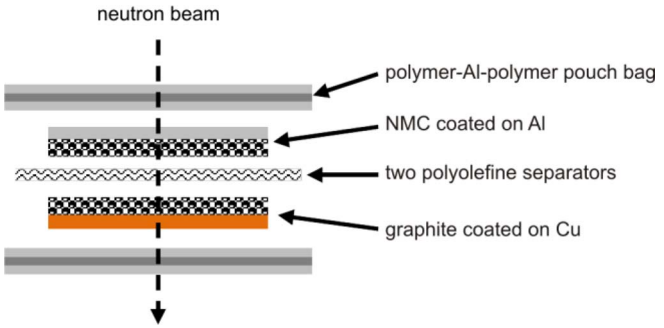

Figure 5. (color online): Schematic drawing of sample pouch cell. A vertical cross section of components in the beam.

should not give rise to large amounts of the total scattering intensity. This is directly visible when looking at our ex situ SANS measurements of individual components of the cell. The components of the pouch bag were evaluated by merging data obtained with all three SANS instrument configurations (high, medium and low Q-range, see experimental details). From Figure 6 we can conclude that the major scattering contributions of a graphite|NMC pouch cell can be attributed to the cathode (red circles) and the anode (gray rectangles), while the entire casing pouch bag contributes only a little amount to the total system scattering (green triangles).

Figure 7 shows a simulation of the full pouch bag cell (red circles), created by adding up the single component data, which is also compared to the obtained scattering signal of a full pouch cell (black rectangles). The prominent curvature of the cathode contribution (Figure 7) is decreased by adding the anode part to the plot in the log-scale. Note the incoherent background (flat straight region at high Q) is increased for the simulated cell because the separator and electrolyte scattering where present in each contribution part (empty cell, single cathode, single anode) while the full cell contains this background only once. The otherwise excellent fit shows that the superposition of the independent scattering subsystems from eq. 9 is a good approximation of the observable experimental pouch battery scattering. We will use this interpretation later in more detail when considering the in situ and especially the in operando experiments. First, however, we used some classical SANS methods to further analyze the data of the single component measurements.

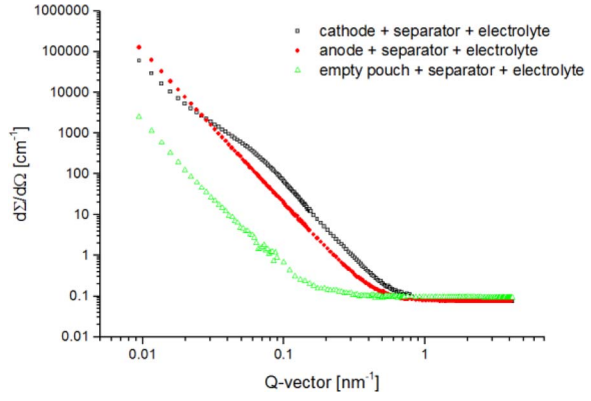

Figure 6. (color online): Differential cross section dΣ/dΩ(Q) vs. Q of single electrodes. Grey rectangles anode, red circles cathode, green triangles empty pouch bag. All single components include separator and electrolyte as background.

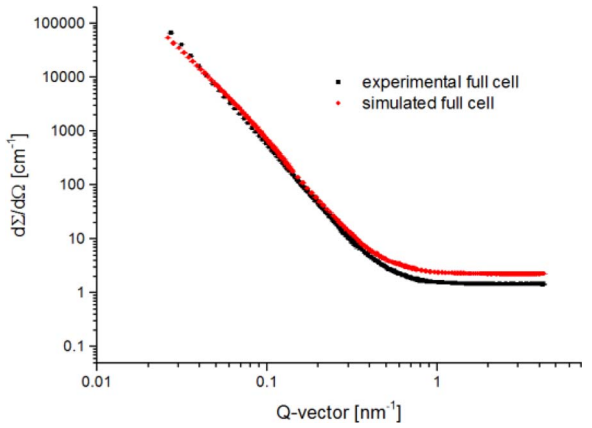

Figure 7. (color online): Differential cross section dΣ/dΩ(Q) vs. Q for single components and full pouch cell. All single measured components were added up to simulate the full pouch cell scattering (red circles). In comparison the experimentally observed full cell data are shown (black rectangles). The small difference at high Q-values results from adding the electrolyte and separator contribution three times when adding up the three single components.

ex situ SANS – cell components.— The empty pouch bag casing data can be fitted with a Porod-like background (eq. 10).

$$\frac{d\Sigma}{d\Omega}(Q) = c_0 + c_1 * Q^{-a} \qquad [10]$$

The slope of the empty cell $a = 3.70$ deviates slightly from an expected Porod-like background ($a = 4$), see Figure 8. This is probably because the pouch bag envelope itself is not just an isotropic scatterer, but obviously has a rough surface fractal microstructure, which gives rise to a decrease in the expected Porod-like background scattering. The parameter c_0 in eq. 10 describes the incoherent background scattering, while the parameters c_1 and a, represent the coherent scattering contributions. Comparison of the total amount of scattering intensity from the single components shows that the impact of the empty envelope is rather small and has no impact on the scattering of the electrode layers.

Single NMC cathode data can similarly be fitted with a superposition of a Porod-background and the scattering of the electrode particles using a structure factor for a mass fractal (see eq. 11). The mass fractal approach is suitable for secondary particle agglomerates consisting of smaller primary particles like NMC material (see

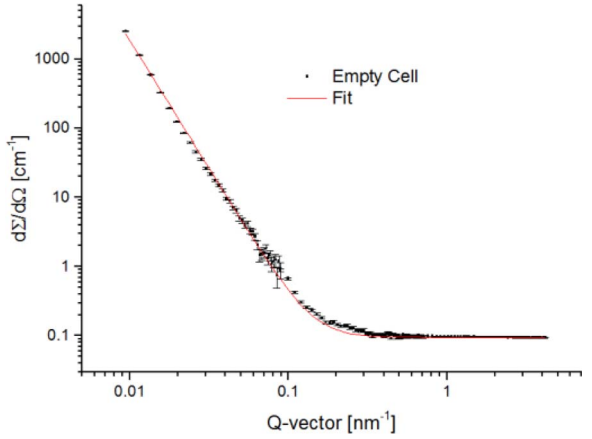

Figure 8. Differential cross section dΣ/dΩ(Q) vs. Q of a measured empty cell with a Porod Fit. Determined fitting parameters: slope $a = 3.70(1)$, $c_0 = 0.0947(3)$ and $c_1 = 7.1(2)\ \text{x}10^{-5}$.

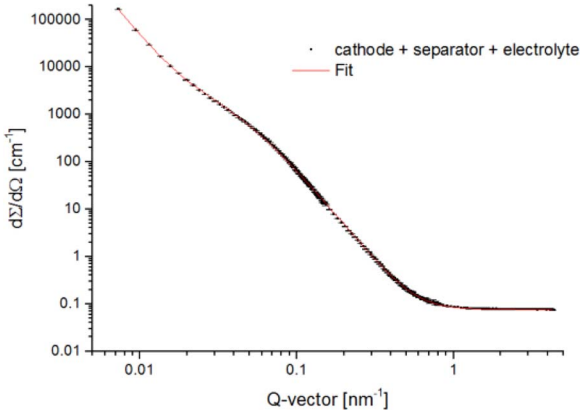

Figure 9. Differential cross section dΣ/dΩ(Q) vs. Q of a measured cathode with a fit of particles using a superposition of Porod-like-background and mass fractal particle distribution, $c_0 = 0.11145(3)$, $c_1 = 0.000250(7)$, a = 4 (fixed), $I_0 = 7070(22)$, D = 2.9544(3) and $R_g = 86.9(1)$ nm.

SEM-picture, Figure 10).

$$\frac{d\Sigma}{d\Omega}(Q) = \frac{I_0 * \sin((D-1)\arctan(Q * x_i))}{(D-1) * Q * x_i (1 + Q^2 x_i^2)^{(D-1)/2)}} \quad [11]$$

Here the parameter D is the dimensionality of the mass fractal, I_0 is the fitted intensity extrapolation for Q(0) and x_i is the size of the fractal particles. By replacing x_i with eq. 12, the radius of gyration (R_g) of the aggregated primary particles can be calculated:

$$x_i^2 = \frac{2R_g^2}{D(D+1)} \quad [12]$$

The obtained mean average radius of gyration $R_g \approx 87$ nm can be converted into equivalent radii of spherical or disc like particles according to:[16]

$$R_{sphere} \approx R_g * \sqrt{\frac{3}{5}} \approx 112\,nm$$

$$R_{disc} \approx R_g * \sqrt{\frac{1}{2}} \approx 123\,nm$$

This yields a mean particle diameter of 2x R_{disc}, or ~250 nm, which compares reasonably well to the primary disc or platelet shaped particles sizes of the NMC-material as observed in SEM images (see. Figure 10). The dimensionality D of the mass fractal is close to 3 which can be expected for a random globular agglomeration of spherical shaped particles.

The raw data of the single anode measurement are shown in Figure 11. We fitted them with a model of a Porod-like background similar to the equation of the empty cell (eq. 10) with a slope of $a = 3.610(5)$. This can be rationalized as the scattering of a fractal surface for which the following relation holds (see e.g.[17,18]):

$$I(Q) \approx Q^{6-D_s} \quad [13]$$

where I(Q) is the scattered intensity, Q the value of the Q-vector and D_s the surface dimension of the fractal. Any surface fractal system will give rise to a slope of 6-D_s in a small-angle scattering experiment in the region of Q where the single particles are too large in size to be resolved individually. While for a smooth surface interface the special case of Porod's approximation is obtained (when $D_s = 2$, then a = 4). Since the large graphitic particles of our samples are in the region 10–50 μm size (see SEM in Figure 12) these large particles cannot be resolved in size with our SANS experiment which is shown by the fact that the curve has a constant slope for the single anode as the scattering from the fractal rough surface of these large particles.

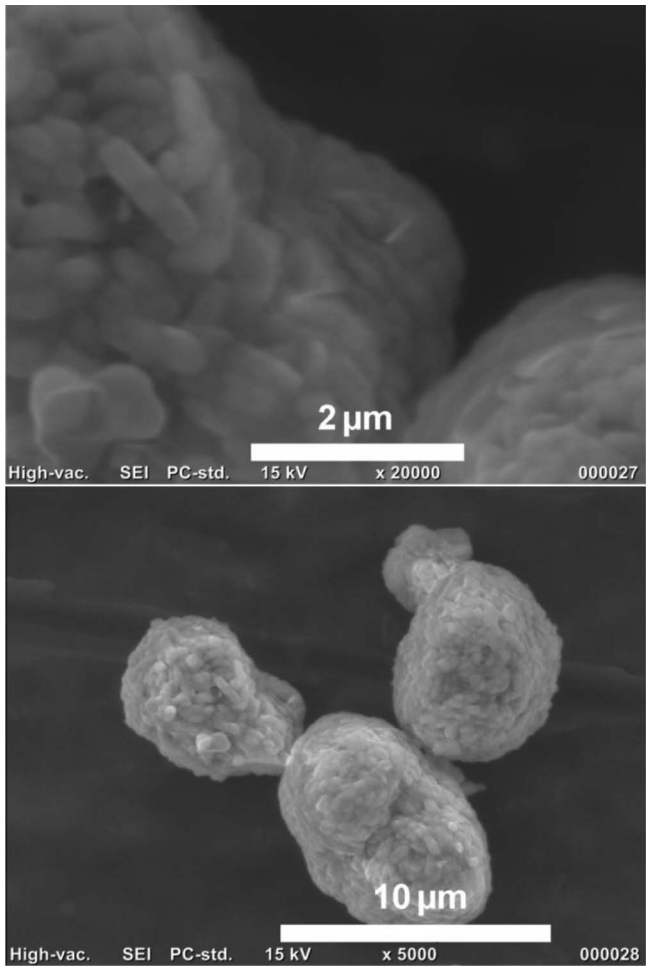

Figure 10. Upper image, SEM picture of NMC raw material agglomerates. Individual primary particles can be distinguished. Lower image, agglomerated globules of primary NMC particles. Picture was taken with a JEOL JCM-6000 SEM, the imaging parameters are shown in the picture.

In situ / in operando SANS.— After characterizing the single cell components, dynamic in operando charge/discharge experiments were performed. Above we used classical fitting of structure/form factor models to the SANS data. In SANS experiments, a change in particle shape or size typically creates shifting peaks in the log-log plots. For the evaluation of the obtained in operando small-angle scattering data, a different approach must be taken. In our case, the direct changes to the intensity vs. Q-vector plot are negligible because the size of the scattering objects is not changing significantly during the in operando study. On the other hand, the scattering contrast factor is changing due to the intercalation of lithium in the active materials, especially in graphite. In Figure 13 we have measured the cell statically in situ just before charging (termed SOC0) and then in the fully charged state (termed SOC100), using all three resolution settings of the SANS-instrument. By the naked eye, the plots are nearly identical, but they differ in detail which is obvious when calculating the difference plot between both. Such a systematic intensity change has been observed earlier (see Wang et al.).[9] In order to analyze these changes more clearly, we convert the cross sections dΣ/dΩ into integrated intensity *A*(Q) (independent from the structure and shape of particles) by integrating the intensity over the measured Q-Range with eq. 14:

$$A(Q) = \int_{q_{min}}^{q_{max}} \frac{d\Sigma}{d\Omega}(Q) \quad [14]$$

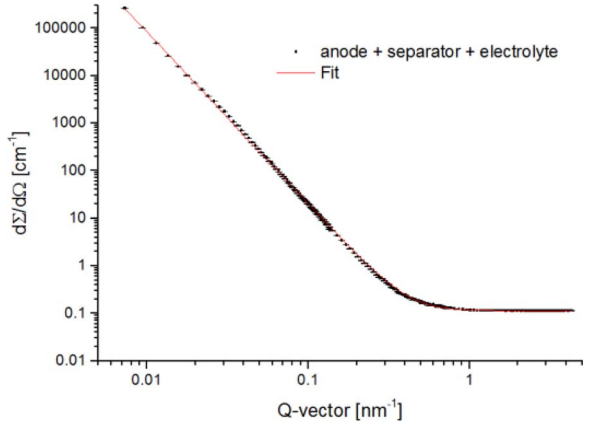

Figure 11. Differential cross section $d\Sigma/d\Omega(Q)$ vs. Q of a measured anode with Porod fit. Refined parameters: slope a = 3.610(5), c_0 = 0.1129(3) and c_1 = 0.0050(1).

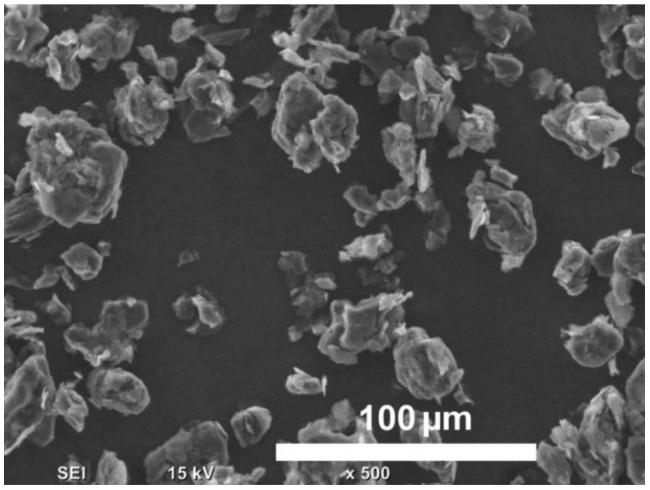

Figure 12. SEM picture of graphite particles. Picture was taken with a JEOL JCM-6000 SEM, the imaging parameters are shown in the picture.

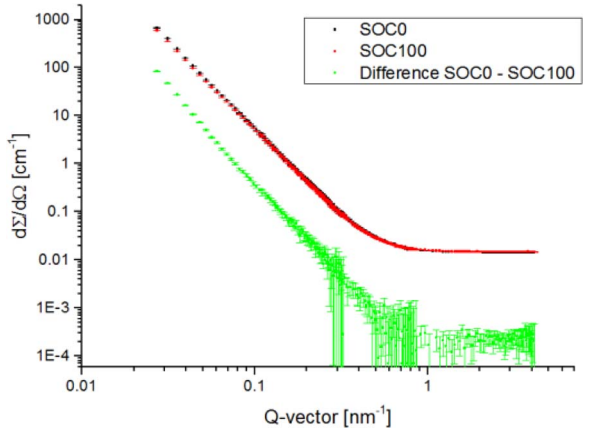

Figure 13. (color online): Differential cross section $d\Sigma/d\Omega(Q)$ vs. Q of a measured fully charged (SOC100) cell with an comparison of an uncharged (SOC0) cell. SOC = state of charge. At high Q the absolute intensities are very low and the differences are small leading to high relative errors. The curves were fitted with a Porod fit (eq. 10). Refined parameters for SOC0, slope a = 3.6712(4), c_0 = 0.014489(6) and c_1 = 0.001179(1); for SOC100, slope a = 3.6387(4), c_0 = 0.014696(6) and c_1 = 0.001174(1).

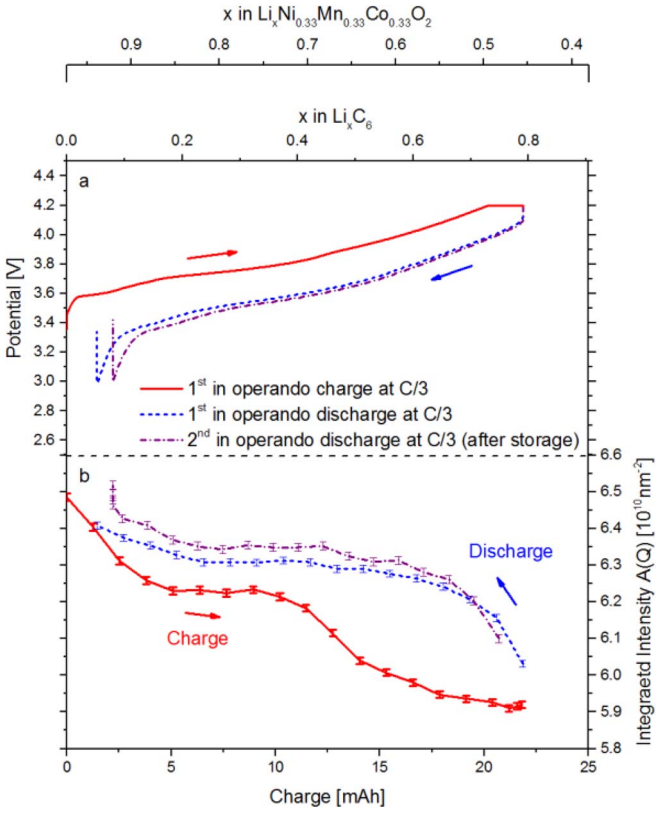

Figure 14. (color online): a) Cell potential and b) integrated intensity $A(q)$ are plotted against charge and electrode utilization. Data for charge and discharge are shown. The red curve represents the initial in operando charge after two formation cycles (see experimental setup for details), followed by the initial discharge (blue curve). The discharge was repeated after three months storage at room temperature in discharged state and subsequent C/3 CCCV charging. Each data point is the integrated intensity of a 10 min time interval of data collection. Electrode utilization was calculated by setting measured charge transfer into relation to theoretical capacities from electrode active material masses (considering only the limiting cathode area for both electrodes). Utilization of NMC was corrected for irreversible losses during formation.

The integrated intensity $A(Q)$ is plotted vs. capacity in Figure 14b. On charging one can observe that the neutron scattering intensity drops continuously until a first plateau is reached after a discharge of ~5 mAh (Figure 14b), which coincides with the onset of the voltage plateau in the charging curve at ~3.7 V (Figure 14a). The integrated intensity decreases from initially 6.48 × 10^{10} nm^{-2} to 6.23 × 10^{10} nm^{-2} at the plateau, corresponding to a ~ 4% drop of its initial value. The end of the plateau coincides with another step in the cell voltage plot at ~3.85 V and the integrated intensity decreases further from 6.23 × 10^{10} nm^{-2} to 5.91 × 10^{10} nm^{-2} until the end of the charging process, corresponding to another ~5% decrease referenced to its initial value. Considering the reversible capacity in the first formation cycle (~21.7 mAh, see Figure 2) and the graphite capacity within the cathode area (~27.6 mAh, see experimental), the lithiation degree of the graphite anode (i.e., x in Li_xC_6) can roughly be estimated, and is plotted along the top x-axis in Figure 14. Based on this estimated lithiation degree, the two initial steps in the cell voltage plot (Figure 14a) seem to be largely caused by the potential dependence of the graphite anode, i.e., by the two initial lithiation stages of lithium intercalation into graphite, for which two distinct voltage plateaus are observed for Li_xC_6 around x~0.1 and x~0.2–0.5.[19] In Figure 17, the potential vs. capacity plot is analyzed further. Half cell measurements of the graphite and NMC electrodes give typical differential plot dV/dQ (Figure 17a), where peaks indicate the step-wise transitions between two-phase plateau regions, which mark the end and beginning of phases in the lithiation process. For graphite and accordingly for the full cell

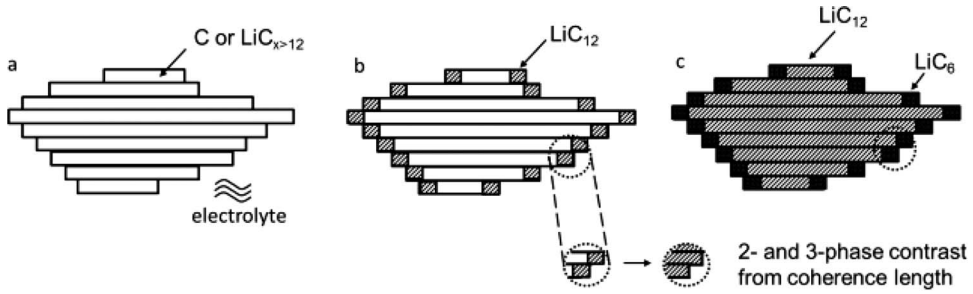

Figure 15. Simplified scheme of interfacial lithiation of a stacked graphite particle. Phases at the surface have a distinct contrast to the surrounding electrolyte. Scattering contrast would vary until the phase thickness reaches ~ ca. 500 nm coherence length. The phase boundary inside the particle has low contrast and can be neglected. Everything beyond this distance from surface is practically invisible for SANS. Three SOCs are shown a) 0% for pristine graphite, b) some % lithiation and c) more than 50% lithiation.

(Figure 17b), we can thus relate the dV/dQ peaks to the onset of formation of Li_xC_6 phases. The three peaks on the left are attributed to the onset of LiC_{24}, LiC_{18} and LiC_{12} formation; the single peak to the right can be attributed to the formation of LiC_6. The first three phases cannot be distinguished by SANS, but correlate to the first step in the integrated intensity, whereas the onset of LiC_6 is clearly related to the second step in the integrated intensity. After charging, the cell was kept for 150 min at OCV. When the discharge is being started after the rest at OCV, the initial integrated intensity is ~2% higher (6.03×10^{10} nm^{-2}) compared to the value directly at the end of the charging, and within another 10 minutes (SANS acquisition time) rises by another ~2% to 6.16×10^{10} nm^{-2}. From there, it gradually increases until it reaches 6.31×10^{10} nm^{-2} at ~5 mAh (or x~0.2). In the final part of the discharge, the integrated intensity rises more rapidly until the final value of 6.41×10^{10} nm^{-2} is reached, which is ~1% below the original value at the beginning of this charge/discharge sequence.

The interpretation of these changes is the following. The initial scattering of the sample, and thus the integrated intensity is dominated, as the preliminary experiments show, by the contrast factor of the anode and cathode active materials. The scattering contribution from these components arises from the contrast of the particles in relation to the surrounding electrolyte matrix. Table II shows the contrast factors relative to the electrolyte for these systems, indicating that the anode contrast factor vs. the electrolyte is nearly a magnitude larger than the contrast factor of any of the other phases. Figure 16 shows the evolution of the contrast factors depending on electrode

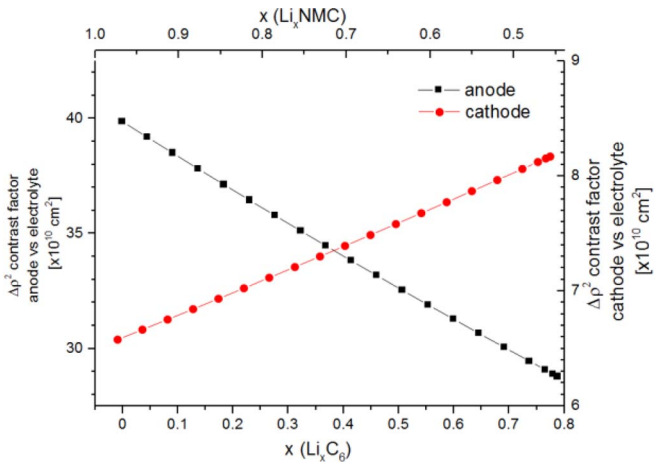

Figure 16. (color online): Evolution of the anode (black squares, left y-axis and bottom x-axis) and cathode (red circles, right y-axis and upper x-axis) versus electrolyte contrast factors during the in operando measurements. The compositional values for Li_xC_6 and Li_xNMC are calculated from the transferred charge capacities.

composition. In Table I and II the compositions of LiNMC/$Li_{0.75}$NMC and $Li_{0.5}$NMC are taken only as example nominal compositions for better showing the trend.

Now let us consider the electrochemical processes inside the cell. During charging, the intercalation reaction starts with pure graphite particles in which Li-ions are intercalated gradually. Examining the change in contrast factor when going from discharged pristine graphite, C, to the half-charged phase LiC_{12} (x = 0.5), we see that the contrast factor of the anode drops relative to the initial value (see Table II). On the contrary, the cathode scattering contrast increases relative to the initial value when going from the Li_1NMC (discharged) to $Li_{0.75}$NMC (partially charged). Since the measured scattering is a superposition of all scattering systems in our sample, as described in eq. 9, the amplitude of the entire cell system is proportional to the relative scattering contrast factors of all components multiplied by the number of particles in the system. If we consider the relative changes of the contrast factors of cathode/electrolyte and anode/electrolyte, we obtain the values calculated in the last column of Table II. The simple difference when going from discharged to half-charged anode ($\Delta\rho^2 = -19\%$) and cathode ($\Delta\rho^2 = +11\%$) sums up to a −8% net decrease of scattering intensity as long as the form and structure factors remain approximately unchanged (i.e., unchanged shape, size, and number of particles in the system). The assumption that form and structure factors are nearly constant in our case seems to be valid, as otherwise we would see directly discrete changes to the scattering in the I(Q) vs. Q plot (see Figure 13). The calculated 8% intensity decrease is the same order of magnitude as the observed decrease of 4% in the integrated intensity vs. capacity plot reached at a charge capacity of ~5 mAh (see Figure 14b). A further net decrease of 10% (anode $\Delta\rho^2 = -34\%$, cathode $\Delta\rho^2 = +24\%$) is calculated when going from half-charged (LiC_{12}) to charged state (LiC_6), while the data show a net decrease of 5%, which is again in the right order of magnitude.

Now we consider the detailed lithiation process during discharge. For NMC it is well established that the phase composition is changing continuously, shown, e.g., in XRD studies by Yabuuchi et al.[20] For a continuously changing contrast factor we would thus expect a linearly changing scattering in SANS (again assuming constant form and structure factors) (see with Fig 16.). However, since the SANS data represent a superposition of cathode and anode scattering contributions, we have to consider the changing contrast factors from the graphite as well. For graphite the situation is more complicated because there are multiple phases, like LiC_{12} and LiC_6 that form gradually and also coexist, as shown for example by neutron diffraction studies.[21] Despite that if we assume a continuous lithiation of the graphite with no discrete phases we would as well obtain a linearly changing scattering length density and as such a linear dependence in the scattering contrast (see Fig. 16).

To understand our SANS data, we also have to consider the coherence length of our SANS experiment, i.e., the length scale on which SANS is sensitive to contrast differences, which is ~500 nm in the configuration used for the in operando studies. This means that SANS is sensitive to inhomogeneities in the distribution of phase domains on

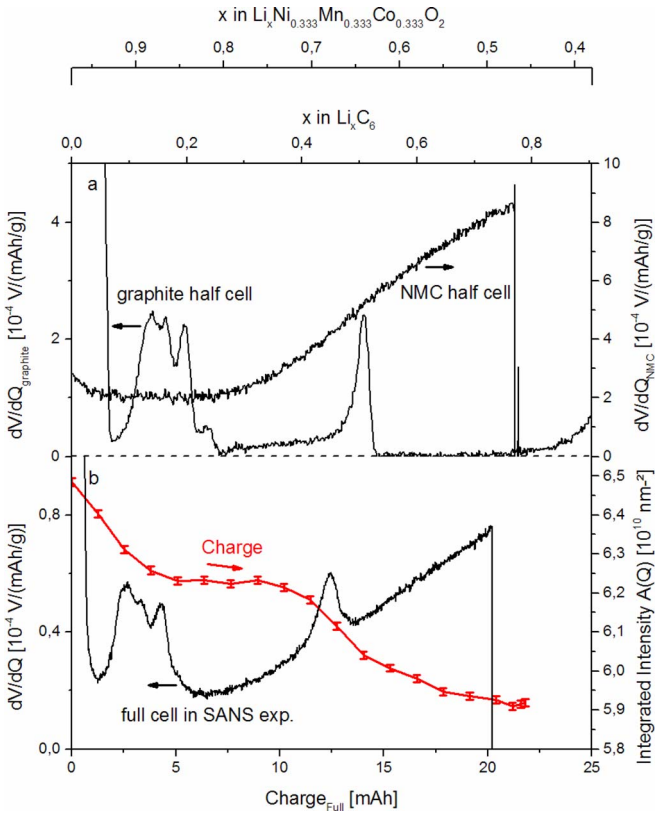

Figure 17. (color online): Plot of differential dV/dQ of potential curve for a graphite half cell (intercalation, loading ca. 2 mAh/cm^2) and a NMC half cell (deintercalation, loading ca. 1.5 mAh/cm^2) cycled at C/10 vs. Li in a coin cell. Steps in the potential vs. capacity plot are indicated by peaks in the differential. b) Plot of differential dV/dQ for the measured pouch full cell during 1st in operando charge at C/3 and in red color related scattering invariant A(Q).

this scale. For the small cathode primary particles (diameter <<500 nm), the SANS signal derives from the entire particle, corresponding to the contrast factor resulting from the calculated average scattering length density. Therefore, this does not contribute to the step-like features in the SANS curve (Fig 14.), as the SANS intensity should otherwise be dropping monotonously.

On the other hand, for the larger graphite particles, this is not the case, since the mean particle diameter is ≈22 μm (volume-averaged diameter, obtained by laser scattering). Thus, the SANS scattering signal from the graphite/electrolyte only derives from interactions in certain parts of the graphite particles.

Based on the above consideration, the SANS data in Figure 14b could be interpreted as deriving from the gradual diffusion of lithium from a first established surface layer at the outside perimeter of the graphite particles into the particle center. Indications of the varying Li concentration along the radial direction of graphite particles during charge and discharge pulses are provided by dynamic battery models.[22–24] In this case, an initial LiC_{12}/C phase boundary (Figure 15b) followed by a LiC_6/LiC_{12} phase boundary (Figure 15c) will move from the surface to the center of graphite particles. Again since SANS is sensitive only to surface layers of ∼500 nm thickness or to phase boundaries in domains of this size, the relevant scattering contributions will thus only be from electrolyte vs. surface layer and from phase boundaries inside the particle.

In Table II, the relevant contrast factors are listed. Lithiated graphite against electrolyte gives us the few % relative contrast change as mentioned above. But the contrast factor of the (non-)lithiated graphite interfaces inside particles is rather low (<1% of the value of graphite) and probably not observed in the integrated intensity plot. This implies that at first the integrated intensity drops linearly, and when all surface regions (within the coherence length) have been transformed to LiC_{12}, the integrated intensity should remain rather constant until all particles are lithiated up to the point of LiC_{12}.

We can now compare the active masses of the whole particle to the active mass in a surface layer of a thickness equal to the coherence length. Then a 500 nm surface shell represents approx. 7% of total active mass. The capacity until the first plateau (∼5 mAh) in relation to the total anode capacity (27.6 mAh opposite of cathode area) is ∼18%. The lower value of the calculated active mass in the shell when compared to the observed values of nearly 18% can be rationalized by the diffusion and presence of some lithium deeper into the particle core and thus lithiated phases LiC_{18} or LiC_{24} are already present beyond the shell which is determining the scattering contrast. The amount of lithium which already moved deeper into the particles is barely giving contrast and thus is nearly invisible.

When all particles are lithiated to LiC_{12} one can expect to see another linear drop in scattering intensity due to the beginning transformation of LiC_{12} to LiC_6 on the particle surface (compare Figure 15b, 15c). Once the particle surfaces are completely transformed the scattering intensity should again remain rather constant until the particles are fully transformed into LiC_6 as the scattering between a shell of LiC_6 and a core of LiC_{12} also gives only a small contrast factor (see contrast factors from Table II).

This is what is observed in our in operando experiment. The evaluation of the discharge plots of integrated intensity vs. capacity reveals another interesting feature. The integrated intensity rises more quickly back to the intermediate plateau which is much longer lasting than in the charging process. Only, shortly before the end of the discharge a further increase of the integrated intensity is observed.

This we interpret as a result of the fact that Li-release out of the particles into the electrolyte seems to be faster than the Li-diffusion into the particles upon intercalation as previously reported by S. R. Sivakkumar et al.[25] This causes a very fast creation of an intermediate LiC_{12} surface yielding an intermediate scattering contribution reflected in the extended intermediate value of the integrated intensity plateau. The contrast between the shrinking LiC_6 in the core and the LiC_{12} shell is again very low. In the end a contrast of a (nearly) pristine graphite shell to surrounding electrolyte is observed.

To confirm the results the experiment was repeated with the same cell after 3 months and the results for discharging were approved not only qualitatively but also quantitatively (see Figure 14b).

Each time the small step in the voltage plot nearly coincides with the beginning of the plateau in the integrated intensity.

Conclusions

We have shown that using in situ neutron small-angle scattering offers the possibility to monitor non-destructively complete pouch bag cells in situ and in operando under real-life working conditions. Together with single component measurements and scattering length density calculations the SANS method can provide a tool to distinguish specific components in operando. With the in situ SANS technique the compositional changes during charging/discharging of a pouch bag cell can be monitored. Although in these first experiments the time resolution was only 10 minutes we estimate that in future experiments the time resolution can be optimized by a factor of 5 or maybe even 10 and thus allow faster measurements on a 1–2 minute time scale. In this case, we would be able to also study the lithium plating kinetics as was done previously by means of neutron diffraction.[21] The phase changes of the active materials are directly correlated to changes of the total integrated intensity in the course of a charge/discharge cycle. We also present a first model to explain the observed intensity changes as a function of gradual particle lithiation. The analysis of scattering contributions from a defined volume given by the coherence length allows to follow the lithiation of active material particles. Due to this local sampling of contrast, core-shell lithiation processes can be monitored. With this method it will be possible to follow the growing respectively movement of the different phase boundaries inside

battery cells non-destructively, using a well-established cell standard (pouch bag single layer cells). Future experiments will be performed to improve and expand the models. This can be reached with studies to monitor the influence of material variations and charging/discharging parameters on the measured SANS data.

Acknowledgment

This research was funded by the BMBF (Federal Ministry of Education and Research, Germany) project "ExZellTUM", grant number 03X4633A. We thank the Heinz Maier-Leibnitz Zentrum (MLZ) for granting us beam time for the experiments. We thank Jörg Schuster for support during the SANS experiments. We thank SGL Carbon GmbH for providing graphite materials.

References

1. M. Anderman, *in* "http://advancedautobat.com/industry-reports/2014-Tesla-report/index.html", www.advancedautobat.com, 2014.
2. J. Vetter, P. Novák, M. R. Wagner, C. Veit, K. C. Möller, J. O. Besenhard, M. Winter, M. Wohlfahrt-Mehrens, C. Vogler, and A. Hammouche, *Journal of Power Sources*, **147**(1–2), 269 (2005).
3. M. Broussely, S. Herreyre, P. Biensan, P. Kasztejna, K. Nechev, and R. J. Staniewicz, *Journal of Power Sources*, **97–98**(0), 13 (2001).
4. M. Broussely, P. Biensan, F. Bonhomme, P. Blanchard, S. Herreyre, K. Nechev, and R. J. Staniewicz, *Journal of Power Sources*, **146**(1–2), 90 (2005).
5. G. Sandi, P. Thiyagarajan, K. A. Carrado, and R. E. Winans, *Chemistry of Materials*, **11**(2), 235 (1999).
6. S. M. Mamun, M. Herstedt, K. Oikawa, T. Gustafsson, T. Otomo, M. Furusaka, T. Kamiyama, H. Sakaebe, and K. Edström, *Applied Physics A*, **74**(1), 1028 (2002).
7. C. A. Bridges, X.-G. Sun, J. Zhao, M. P. Paranthaman, and S. Dai, *The Journal of Physical Chemistry C*, **116**(14), 7701 (2012).
8. M. Nagao, C. Pitteloud, T. Kamiyama, T. Otomo, K. Itoh, T. Fukunaga, K. Tatsumi, and R. Kanno, *Journal of The Electrochemical Society*, **153**(5), A914 (2006).
9. W. Howard, R. G. Downing, A. D. Joseph, and S. H. Daniel, in *Polymers for Energy Storage and Delivery: Polyelectrolytes for Batteries and Fuel Cells*, Vol. 1096, p. 91, American Chemical Society, (2012).
10. D. Aurbach, B. Markovsky, I. Weissman, E. Levi, and Y. Ein-Eli, *Electrochimica Acta*, **45**(1–2), 67 (1999).
11. R. Gilles, A. Ostermann, C. Schanzer, B. Krimmer, and W. Petry, *Physica B*, **385–86**, 1174 (2006).
12. R. Gilles, A. Ostermann, and W. Petry, *J Appl Crystallogr*, **40**, S428 (2007).
13. R. Gilles, A. Heinemann, S. Mühlbauer, and H. Eckerlebe, SANS-1 instrument schematics & technical description, http://www.mlz-garching.de/sans-1, Last Accessed, 30.10.2014.
14. G. Kostorz, *Neutron scattering*, Academic Press, New York (1979).
15. I. Grillo, in *Soft Matter Characterization*, R. Borsali and R. Pecora, eds., p. 723, Springer, Netherlands, (2008).
16. V. Gerold, *Z. angew. Phys.*, **9**, 43 (1957).
17. J. Teixeira, *J Appl Crystallogr*, **21**(6), 781 (1988).
18. P. W. Schmidt, *J Appl Crystallogr*, **24**(5), 414 (1991).
19. J. R. Dahn, *Physical Review B*, **44**(17), 9170 (1991).
20. N. Yabuuchi and T. Ohzuku, *Journal of Power Sources*, **119–121**, 171 (2003).
21. V. Zinth, C. von Lüders, M. Hofmann, J. Hattendorff, I. Buchberger, S. Erhard, J. Rebelo-Kornmeier, A. Jossen, and R. Gilles, *Journal of Power Sources*, **271**(0), 152 (2014).
22. A. Nyman, T. G. Zavalis, R. Elger, M. Behm, and G. Lindbergh, *Journal of the Electrochemical Society*, **157**(11), A1236 (2010).
23. D. M. Bernardi and J. Y. Go, *Journal of Power Sources*, **196**(1), 412 (2011).
24. T. F. Fuller, M. Doyle, and J. Newman, *Journal of The Electrochemical Society*, **141**(1), 1 (1994).
25. S. R. Sivakkumar, J. Y. Nerkar, and A. G. Pandolfo, *Electrochimica Acta*, **55**(9), 3330 (2010).
26. J. Kohlbrecher, *SASfit Software*, (2014).
27. O. Dolotko, A. Senyshyn, M. J. Mühlbauer, K. Nikolowski, F. Scheiba, and H. Ehrenberg, *Journal of The Electrochemical Society*, **159**(12), A2082 (2012).